J Eng Math (2009) 64:331–351
DOI 10.1007/s10665-009-9275-1

Analysing the pattern of pulse waves in arterial networks: a time-domain study

J. Alastruey · K. H. Parker · J. Peiró · S. J. Sherwin

Received: 24 April 2008 / Accepted: 9 February 2009 / Published online: 27 February 2009

Abstract The mechanisms underlying the shape of pulse waves in the systemic arterial network are studied using the time-domain, one-dimensional (1-D) equations of blood flow in compliant vessels. The pulse waveform at an arbitrary location in the network is initially separated into a peripheral component that depends on the cardiac output, total compliance and total peripheral resistance of the network, and a conduit component governed by reflections at the junctions of the large conduit arteries and at the aortic valve. The dynamics of the conduit component are then analysed using a new algorithm that describes all the waves generated in the linear 1-D model network by a single wavefront starting at the root. This algorithm allows one to systematically follow all the waves arriving at the measuring site and identify all the reflection sites that these waves have visited. Application of this method to the pulse waves simulated using a 1-D model of the largest 55 systemic arteries in the human demonstrates that peripheral components make a larger contribution to aortic pressure waveforms than do the conduit components. Conduit components are closely related to the outflow from the left ventricle in early systole. Later in the cardiac cycle, they are the result of reflections at the arterial junctions and aortic valve. The number of reflected waves increases approximately as 3^m, with m being the number of reflection sites encountered. The pressure changes associated with these waves can be positive or negative but their absolute values tend to decrease exponentially. As a result, wave activity is minimal during late diastole, when the peripheral components of pressure and the flow are dominant, and aortic pressures tend to a space-independent value determined by the cardiac output, total compliance and total peripheral resistance. The results also suggest that pulse-wave propagation is the mechanism by which the arterial system reaches the mean pressure dictated by the cardiac output and total resistance that is required to perfuse the microcirculation. The total compliance determines the rate at which this pressure is restored when the system has departed from its equilibrium state of steady oscillation. This study provides valuable information on

J. Alastruey (✉) · J. Peiró · S. J. Sherwin
Department of Aeronautics, Imperial College London, South Kensington Campus, SW7 2AZ London, UK
e-mail: jordi.alastruey-arimon@imperial.ac.uk

J. Alastruey · K. H. Parker
Department of Bioengineering, Imperial College London, South Kensington Campus, SW7 2AZ London, UK
e-mail: k.parker@imperial.ac.uk

J. Peiró
e-mail: j.peiro@imperial.ac.uk

S. J. Sherwin
e-mail: s.sherwin@imperial.ac.uk

identifying and measuring the parameters and pathways of the arterial network that have the largest effect on the simulated pulse waveforms.

Keywords Arterial pulse waveforms · Diastolic decay · Dicrotic notch · One-dimensional modelling · Wave tracking algorithm

1 Introduction

Pulse waveforms carry information about the morphology and functionality of the cardiovascular system. Therefore, a good understanding of the mechanics of pulse wave propagation in normal conditions and the impact of disease and anatomical variations on the patterns of propagation can provide valuable information for clinical diagnosis and treatment. Several comparisons against in vivo [1,2] and in vitro [3, Chap. 3], [4] data have shown the ability of the nonlinear one-dimensional (1-D) equations of blood flow in compliant vessels [5–10] to capture the main features of pressure and flow waveforms in large arteries. Indeed, arterial pulse wavelengths are sufficiently long compared to arterial diameters to justify the use of a 1-D rather than a three-dimensional (3-D) approach when a global and sectionally averaged assessment of blood flow in the arterial system is required.

The shape of the arterial pulse wave is continuously altered as it propagates from central (or conduit) to peripheral arteries. According to the 1-D formulation, pulse waveforms depend on the geometry, local pulse wave speeds (or distensibilities), velocity profiles, and boundary conditions of the arterial network. Imaging techniques such as computer tomography, magnetic resonance and ultrasound are now able to provide patient-specific information on vessel geometry and the inflow waveform at the root of the arterial model (typically at the ascending aorta), as well as more limited information on pulse wave speeds and local velocity profiles. Outflow boundary conditions can be estimated from pressure and flow data that can be measured in vivo [11]. These techniques permit the use of the 1-D model to quickly and accurately simulate pulse waveforms, potentially under patient-specific conditions, in vessels that cannot be assessed in vivo for technical and physiological reasons, such as the inability to access vessels of interest and isolate variables without compensatory effects of cardiovascular homeostatic reflexes. Examples of clinically relevant problems studied using the 1-D formulation are [2,7,12–16]. Moreover, the 1-D model can also be used to provide the boundary conditions for 3-D flow simulations [17,18].

Full understanding of the mechanisms that produced the simulated pulse waveforms, however, remains an open problem. It has been shown [19–21] that separation of the pressure waveform into a space-independent reservoir component, generated by the windkessel effect, and a wave component, which varies with time and distance along the arteries, allows a better interpretation of the mechanics behind the typical pulse waveforms in the systemic circulation. However, the physical bases of this separation have not been yet established, and the relation between the shape of the wave components and the local features of the complex arterial network remains to be studied in detail. It would be particularly useful to determine the physical properties of the cardiovascular system that contribute to the pattern of pulse waves throughout the cardiac cycle, which should elucidate those properties to be monitored to diagnose disease and those to be targeted to prevent and treat disease.

In this work, we investigate the mechanisms that produce the patterns of systemic arterial pulse waves using a time-domain analysis of the linear 1-D equations. In particular, we are interested in identifying the properties of the system that dictate the dicrotic notch typically observed in the pressure waveform at the end of systole (the phase of the heartbeat when the heart contracts and ejects blood into the ascending aorta, $T_0 \leq t \leq T_N$) and the pressure decay during diastole (the phase of the heartbeat when the heart relaxes and the aortic valve is closed, $T_N \leq t \leq T_f$) (Fig. 1, right). Section 2 introduces the 1-D formulation and Sects. 3–5 show the novel method proposed in this work to separate and analyse the contributions from different parts of the arterial network to the pressure and flow waveforms at an arbitrary location. Section 3 establishes the relation between the 1-D formulation and Frank's windkessel model [22], and studies the contributions from the peripheral flow dynamics. Section 4 analyses the reflections produced by the boundary condition at the inlet of the ascending aorta, which models the dynamics of the outflow from the left ventricle through the aortic valve. Finally, Sect. 5 focuses on the flow dynamics in the

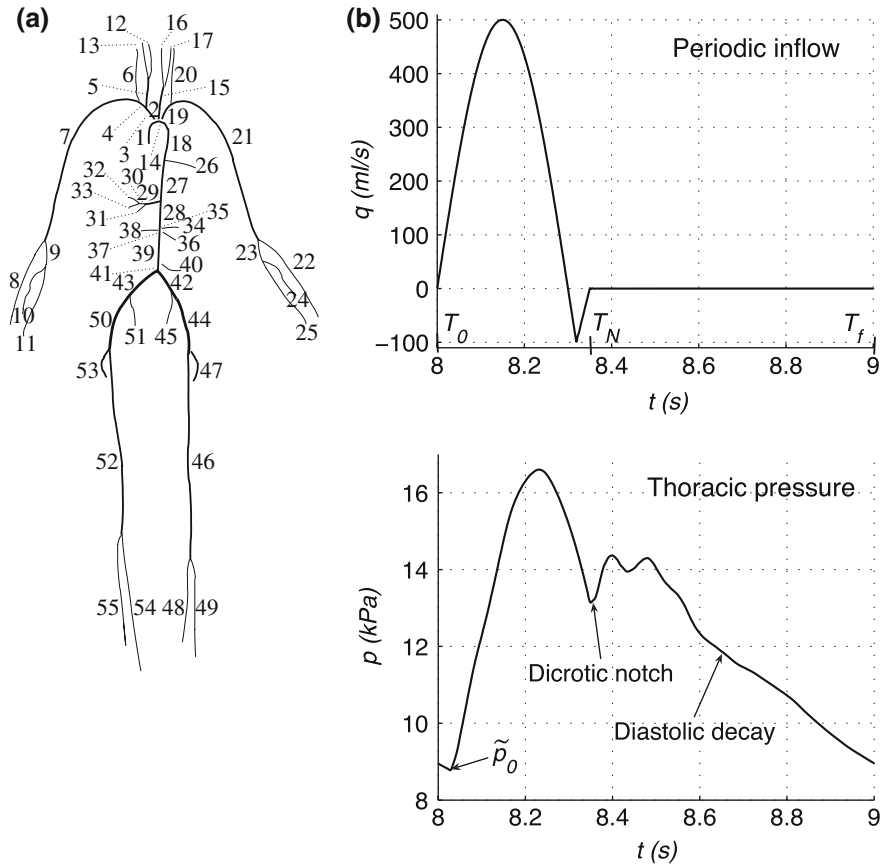

Fig. 1 (*left*) Connectivity of the largest 55 systemic arteries in the human, as proposed in [12]. Their names and properties are shown in Tables 1 and 2. (*top right*) Periodic inflow rate imposed at the inlet of the ascending aorta (segment 1). T_0, T_N, and T_f are the times when systole starts, systole ends, and diastole ends, respectively. (*bottom right*). Pressure in the thoracic aorta (midpoint of segment 18) once the flow has reached a periodic state. $\tilde{p}_0$ is the diastolic pressure

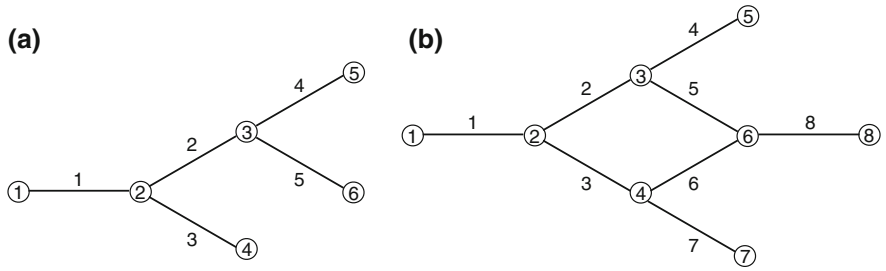

Fig. 2 Networks used to illustrate the wave-tracking analysis: (*left*) a tree with six nodes ($N = 6$) and five edges ($E = 5$), and (*right*) a network containing a loop with $N = 8$ and $E = 8$. Table 3 shows the geometrical properties of both networks

conduit arteries controlled by wave reflections at the arterial junctions, and proposes a new algorithm to describe all the waves generated in a linear, 1-D model network by a single wavefront starting at the root. This *wave tracking algorithm* allows us to systematically follow all the waves generated at an arbitrary measuring site and identify all the reflection sites that these waves have visited. The networks shown in Figs. 1 and 2 will be used to illustrate this analysis.

2 1-D formulation

Conservation of mass and balance of momentum applied to a 1-D impermeable and deformable tubular control volume of Newtonian incompressible fluid leads to the nonlinear system of hyperbolic partial differential equations [10]

$$\frac{\partial A}{\partial t} + \frac{\partial (AU)}{\partial x} = 0, \tag{1}$$

$$\frac{\partial U}{\partial t} + U\frac{\partial U}{\partial x} + \frac{1}{\rho}\frac{\partial P}{\partial x} = \frac{f}{\rho A}, \tag{2}$$

where x is the axial coordinate along the vessel, t is the time, $A(x,t)$ is the cross-sectional area of the lumen, $U(x,t)$ is the average axial velocity, $P(x,t)$ is the average internal pressure over the cross-section, and $\rho = 1{,}050\,\mathrm{Kg\,m^{-3}}$ is the density of blood. The friction force per unit length f is given by $f = -2(\gamma+2)\mu\pi U$, where $\mu = 4\,\mathrm{mPa\,s}$ is the viscosity of blood and γ is a non-dimensional correction factor that depends on the assumed velocity profile. Following [7], $\gamma = 9$ is a good compromise fit to the experimental data. Note that $\gamma = 2$ corresponds to a parabolic profile which leads to the Poiseuille's flow resistance $f = -8\mu\pi U$. The system of governing equations can be completed with the tube law [1,2,8,10]

$$P = \frac{\beta}{A_0}\left(\sqrt{A} - \sqrt{A_0}\right), \qquad \beta(x) = \frac{4}{3}\sqrt{\pi}hE, \tag{3}$$

which assumes a thin, homogeneous, incompressible and elastic arterial wall, in which each cross-section is independent of the others, with a thickness $h(x)$, a Young's modulus $E(x)$, and a lumen area $A_0(x)$ at the reference state $(P, U) = (0, 0)$.

Riemann's method of characteristics applied to Eqs. 1 to 3 shows that changes in pressure and velocity are propagated forward (in the positive direction of x) by W_f and backward (in the negative direction of x) by W_b along the characteristic curves $\mathrm{d}\hat{x}_{f,b}/\mathrm{d}t = U \pm c$, respectively, where $\hat{x}_{f,b}(t)$ represent curves in the (x,t) space, $W_{f,b} = U \pm 4(c - c_0)$ are the characteristic or Riemann variables, $c = \sqrt{\beta/2\rho A_0}A^{1/4}$ is the pulse wave speed, and $c_0 = c(A_0)$. If $f = 0$ and β and A_0 are constant, $W_{f,b}$ are invariant along the characteristic curves [11].

2.1 Linear formulation

To simplify the analysis of pulse waveforms to be described in Sects. 3–5, we express Eqs. 1 and 2 in terms of the (A, P, Q) variables, with $Q = AU$, and we linearise them together with Eq. 3 about the reference state $(A, P, Q) = (A_0, 0, 0)$, with β and A_0 constant along x, to obtain

$$\begin{cases} C_{1D}\dfrac{\partial p}{\partial t} + \dfrac{\partial q}{\partial x} = 0, \\ L_{1D}\dfrac{\partial q}{\partial t} + \dfrac{\partial p}{\partial x} = -R_{1D}q, \\ p = \dfrac{a}{C_{1D}}, \end{cases} \tag{4}$$

where a, p and q are the perturbation variables for area, pressure and flow rate, respectively, i.e., $(A, P, Q) = (A_0 + a, p, q)$, and

$$R_{1D} = \frac{2(\gamma+2)\pi\mu}{A_0^2}, \qquad L_{1D} = \frac{\rho}{A_0}, \qquad C_{1D} = \frac{A_0}{\rho c_0^2} \tag{5}$$

are the viscous resistance to flow, blood inertia and wall compliance, respectively, per unit of length of vessel. Applying the method of characteristics, system (4) can be written as

$$\frac{\partial w_f}{\partial t} + c_0\frac{\partial w_f}{\partial x} = -\frac{R_{1D}}{L_{1D}}q, \quad \frac{\partial w_b}{\partial t} - c_0\frac{\partial w_b}{\partial x} = -\frac{R_{1D}}{L_{1D}}q, \tag{6}$$

where

$$w_{f,b} = q \pm \frac{p}{Z_0}, \quad Z_0 = \frac{\rho c_0}{A_0} \tag{7}$$

are the linear Riemann variables, Z_0 is the characteristic impedance of the vessel, and $c_0 = \sqrt{1/L_{1D}C_{1D}}$ is the linearized pulse wave speed. The set of equations (6) show that linear changes in pressure and flow are propagated forward by w_f and backward by w_b along the characteristic lines $\mathrm{d}\tilde{x}_{f,b}/\mathrm{d}t = \pm c_0$, respectively, where $\tilde{x}_{f,b}(t)$ represent lines in the (x, t) space. If viscous dissipation is neglected ($R_{1D} = 0$), Eq. 6 forms a system of decoupled equations in w_f and w_b, which are invariant along the characteristic lines. The variables w_f and w_b allow us to derive the coefficients that reflect and transmit pulse waves at the junctions and boundaries of the arterial network, as described in the following sections. These coefficients are the direct analogy to the coefficients commonly applied in acoustics and surface waves [10, 23, Chap. 8].

According to Eq. 7, p and q can be written in terms of w_f and w_b as follows

$$p = \frac{w_f - w_b}{2} Z_0, \quad q = \frac{w_f + w_b}{2}. \tag{8}$$

Eq. 8 shows that p and q can be separated into forward and backward components,

$$\begin{gathered} p = p_f + p_b, \quad q = q_f + q_b, \\ p_f = Z_0 w_f/2, \quad p_b = -Z_0 w_b/2, \quad q_f = w_f/2, \quad q_b = w_b/2, \end{gathered} \tag{9}$$

so that changes in p_f and q_f are propagated in the forward direction by w_f, whereas changes in p_b and q_b are propagated backward by w_b.

We solve the inviscid form of system (4) ($R_{1D} = 0$) in the arterial networks shown in Figs. 1 and 2 using a discontinuous Galerkin scheme with a spectral/*hp* spatial discretisation, a second-order Adams–Bashforth time-integration scheme, and the initial conditions $(a, p, q) = (0, 0, 0)$ everywhere in the 1-D model arteries. At the arterial junctions we enforce conservation of mass and continuity of pressure.

Figure 1 (top right) shows the periodic inflow boundary condition (with a mean value of 93 ml/s) imposed at the ascending aorta of the 55-arteries model, which will be described in Sect. 4. Terminal branches are coupled to peripheral windkessel models as will be described in Sect. 3.1. Table 1 shows the geometrical data and wave speeds of each arterial segment, and Table 2 shows the peripheral resistances and compliances of the terminal branches. They are based on the data in [12].

Further details on the 1-D model and its numerical solution are given in [10,11].

Table 1 Lengths, initial radii, and wave speeds of the 55-arteries network in Fig. 1

Arterial segment	Length (cm)	Radius (mm)	c_0 (m/s)	R_{inlet}	R_{outlet}
1. Ascending aorta	4.0	14.5	4.3	–	0.1
2. Aortic arch I	2.0	11.2	4.3	−0.3	0.0
3. Brachiocephalic	3.4	6.2	4.6	−0.8	0.2
4. R. subclavian	3.4	4.2	5.1	−0.5	0.2
5. R. common carotid	17.7	3.7	5.3	−0.6	0.8
6. R vertebral	14.8	1.9	9.0	−0.9	–
7. R. brachial	42.2	3.2	5.9	−0.4	0.4
8. R. radial	23.5	1.6	9.5	−0.8	–
9. R ulnar I	6.7	2.2	8.4	−0.6	0.1
10. R. interosseous	7.9	0.9	14.3	−0.9	–
11. R. ulnar II	17.1	1.9	8.9	−0.2	–
12. R. internal carotid	17.7	1.3	10.7	−0.9	–

Table 1 continued

Arterial segment	Length (cm)	Radius (mm)	c_0 (m/s)	R_{inlet}	R_{outlet}
13. R. external carotid	17.7	1.3	10.3	−0.9	–
14. Aortic arch II	3.9	10.7	4.2	−0.1	0.0
15. L. common carotid	20.8	3.7	5.3	−0.9	0.8
16. L. internal carotid	17.7	1.3	10.7	−0.9	–
17. L. external carotid	17.7	1.3	10.3	−0.9	–
18. Thoracic aorta I	5.2	10.0	4.3	−0.1	0.4
19. L. subclavian	3.4	4.2	5.1	−0.9	0.2
20. L vertebral	14.8	1.9	9.0	−0.9	–
21. L. brachial	42.2	3.2	5.9	−0.4	0.4
22. L. radial	23.5	1.6	9.5	−0.8	–
23. L. ulnar I	6.7	2.2	8.4	−0.6	0.1
24. L. interosseous	7.9	0.9	14.3	−0.9	–
25. L. ulnar II	17.1	1.9	8.9	−0.2	–
26. Intercostals	8.0	1.8	6.8	−1.0	–
27. Thoracic aorta II	10.4	6.6	5.0	−0.5	−0.1
28. Abdominal aorta I	5.3	6.1	5.0	−0.2	−0.2
29. Celiac I	1.0	3.9	5.2	−0.7	0.4
30. Celiac II	1.0	2.0	7.3	−0.7	−0.5
31. Hepatic	6.6	2.2	6.0	−0.6	–
32. Gastric	7.1	1.8	6.4	−0.6	–
33. Splenic	6.3	2.8	5.7	0.1	–
34. Superior mesenteric	5.9	4.4	5.1	−0.6	–
35. Abdominal aorta II	1.0	6.0	4.7	−0.2	−0.1
36. L. renal	3.2	2.6	5.8	−0.9	–
37. Abdominal aorta III	1.0	5.9	4.7	−0.1	0.0
38. R. renal	3.2	2.6	5.8	−0.8	–
39. Abdominal aorta IV	10.6	5.6	4.7	−0.1	0.0
40. Inferior mesenteric	5.0	1.6	6.7	−0.9	–
41. Abdominal aorta V	1.0	5.2	4.5	−0.1	0.1
42. R. common iliac	5.8	3.6	5.3	−0.5	0.2
43. L. common iliac	5.8	3.6	5.3	−0.5	0.2
44. L. external iliac	14.4	3.0	7.7	−0.4	0.0
45. L. internal iliac	5.0	2.0	11.5	−0.8	–
46. L. femoral	44.3	2.2	8.6	−0.5	0.2
47. L. deep femoral	12.6	2.2	8.4	−0.5	–
48. L. posterior tibial	32.1	1.9	12.4	−0.4	–
49. L. anterior tibial	34.3	1.3	14.1	−0.8	–
50. R. external iliac	14.4	3.0	7.7	−0.4	0.0
51. R. internal iliac	5.0	2.0	11.5	−0.8	–
52. R. femoral	44.3	2.2	8.6	−0.5	0.2
53. R. deep femoral	12.6	2.2	8.4	−0.5	–
54. R. posterior tibial	32.1	1.9	12.4	−0.4	–
55. R. anterior tibial	34.3	1.3	14.1	−0.8	–

They are based on the data provided in [12]. The last two columns show the reflection coefficients at the inlet and outlet of the segments connected to junctions

Table 2 Peripheral resistances and compliances at the terminal branches of the 55-arteries network in Fig. 1

Arterial segment	R (10^{10} Pa s m^{-3})	C (10^{-10} m^3 Pa^{-1})
6. R vertebral	0.60	0.62
8. R. radial	0.53	0.70
10. R. interosseous	8.43	0.04
11. R. ulnar II	0.53	0.70
12. R. internal carotid	1.39	0.27
13. R. external carotid	1.39	0.27
16. L. internal carotid	1.39	0.27
17. L. external carotid	1.39	0.27
20. L vertebral	0.60	0.62
22. L. radial	0.53	0.70
24. L. interosseous	8.43	0.04
25. L. ulnar II	0.53	0.70
26. Intercostals	0.14	2.68
31. Hepatic	0.36	1.02
32. Gastric	0.54	0.69
33. Splenic	0.23	1.60
34. Superior mesenteric	0.09	4.00
36. L. renal	0.11	3.29
38. R. renal	0.11	3.29
40. Inferior mesenteric	0.69	0.54
45. L. internal iliac	0.79	0.47
47. L. deep femoral	0.48	0.78
48. L. posterior tibial	0.48	0.78
49. L. anterior tibial	0.56	0.67
51. R. internal iliac	0.79	0.47
53. R. deep femoral	0.48	0.78
54. R. posterior tibial	0.48	0.78
55. R. anterior tibial	0.56	0.67

In all these branches $P_{\text{out}} = 0$

3 Peripheral dynamics

This section studies the effect on arterial pulse waveforms of the resistance and compliance of vessels downstream the largest arteries of the network. We first analyse the local effect on a terminal 1-D model artery (Sect. 3.1) and the global effect involving all the arterial segments of the network (Sect. 3.2). Then, we show how to separate the contribution of peripheral resistances and compliances to the pressure and flow waveforms at any location in the arterial network, and we apply this separation to the pulse waves obtained using the 55-arteries model (Sect. 3.3).

3.1 Local peripheral dynamics

We have previously shown [11] that a single resistance R coupled to the outflow of a 1-D model terminal segment relates w_f and w_b through

$$w_b = -R_t w_f - \frac{2P_{\text{out}}}{R + Z_0}, \quad R_t = \frac{R - Z_0}{R + Z_0}, \tag{10}$$

where R_t is the terminal reflection coefficient, Z_0 is the characteristic impedance of the terminal segment and P_{out} is the pressure at which flow to the venous system ceases. The coefficient R_t is also found in the acoustics and surface-waves literature [23, Chap. 8], and relates the pressure change associated with the reflected wave to that of the incident wave. Equation 10 shows that any incident wave is completely absorbed by the outflow if $R = Z_0$ ($R_t = 0$).

Our study in [11] also showed that a resistance equal to Z_0 is required to match the propagation of forward-travelling waves when a terminal 1-D model artery is coupled to a peripheral compliance C and resistance R. Significant non-physiological reflected waves are generated by the CR model unless the resistance Z_0 is included, resulting in a matched RCR model.

3.2 Global peripheral dynamics

Integration of (4) along the length l of an arterial segment in which $x \in [0, l]$ leads to

$$\begin{cases} C_{0D}\dfrac{\mathrm{d}\hat{p}}{\mathrm{d}t} + q_{\text{out}} - q_{\text{in}} = 0, \\ \\ L_{0D}\dfrac{\mathrm{d}\hat{q}}{\mathrm{d}t} + p_{\text{out}} - p_{\text{in}} = -R_{0D}\hat{q}, \end{cases} \tag{11}$$

where $q_{\text{in}}(t) = q(0, t)$, $q_{\text{out}}(t) = q(l, t)$, $p_{\text{in}}(t) = p(0, t)$ and $p_{\text{out}}(t) = p(l, t)$ are the flow rates and pressures at the inlet and outlet of the segment, $R_{0D} = R_{1D}l$, $L_{0D} = L_{1D}l$, $C_{0D} = C_{1D}l$, and

$$\hat{p}(t) = \frac{1}{l}\int_0^l p\,\mathrm{d}x, \quad \hat{q}(t) = \frac{1}{l}\int_0^l q\,\mathrm{d}x$$

are the mean pressure and flow rate over the whole segment.

Equation 11 applies to each segment i ($i = 1, \ldots, N$) of a bifurcating tree arterial network with N segments and M outflows ($M < N$); i.e.

$$\begin{cases} C^i_{0D}\dfrac{\mathrm{d}\hat{p}_i}{\mathrm{d}t} + q^i_{\text{out}} - q^i_{\text{in}} = 0, \\ \\ L^i_{0D}\dfrac{\mathrm{d}\hat{q}_i}{\mathrm{d}t} + p^i_{\text{out}} - p^i_{\text{in}} = -R^i_{0D}\hat{q}_i, \end{cases} \qquad i = 1, \ldots, N, \tag{12}$$

where the index i indicates the number of the segment. Applying conservation of mass at the junctions of the network, the N equations of conservation of mass in system (12) combine to produce

$$q_{\text{IN}} = \sum_{j=1}^{M} q^j_{\text{out}} + \sum_{i=1}^{N} C^i_{0D}\frac{\mathrm{d}\hat{p}_i}{\mathrm{d}t}, \tag{13}$$

where $q_{\text{IN}}(t)$ is the flow rate at the root of the network. Assuming that $R^i_{0D} = 0$ (see [1]) and $L^i_{0D} = 0$ (see [2]) ($i = 1, \ldots, N$), we have that the N equations of balance of momentum in system (12) lead to $\tilde{p} = p^i_{\text{in}} = p^i_{\text{out}} = \hat{p}_i$, ($i = 1, \ldots, N$), where $\tilde{p}$ is the space-independent pressure to which the 1-D model pressures in system (4) approach as pulse wave activity decreases. Under these conditions, Eq. 13 leads to

$$q_{\text{IN}} = \sum_{j=1}^{M} q^j_{\text{out}} + C_c\frac{\mathrm{d}\tilde{p}}{\mathrm{d}t}, \tag{14}$$

[1] The greatest fall in mean pressure occurs in the arterioles in normal physiological conditions [24, Chap. 12].

[2] In the limit $L^i_{0D} \to 0$ then $c^i_0 = \sqrt{1/L^i_{0D}C^i_{0D}} \to \infty$; i.e. changes in pressure and velocity occur synchronously.

where

$$C_c = \sum_{i=1}^{N} C_{0D}^i \tag{15}$$

is the total conduit compliance.

If each terminal branch $j = 1, \ldots, M$ is coupled to a matched RCR windkessel model relating q_{out}^j to p_{out}^j through [11]

$$q_{\text{out}}^j \left(1 + \frac{Z_0^j}{R_j}\right) + C_j Z_0^j \frac{\mathrm{d}q_{\text{out}}^j}{\mathrm{d}t} = \frac{p_{\text{out}}^j - P_{\text{out}}}{R_j} + C_j \frac{\mathrm{d}p_{\text{out}}^j}{\mathrm{d}t}, \tag{16}$$

with a peripheral resistance R_j, compliance C_j, characteristic impedance Z_0^j, and $p_{\text{out}}^j = \tilde{p}$ $(j = 1, \ldots, M)$ when $R_{0D}^i = L_{0D}^i = 0$ $(i = 1, \ldots, N)$, then Eq. 14 yields

$$q_{\text{IN}} = q_{\text{OUT}} + C_T \frac{\mathrm{d}\tilde{p}}{\mathrm{d}t}, \tag{17}$$

$$q_{\text{OUT}} = \frac{\tilde{p} - P_{\text{out}}}{R_T} - \sum_{j=1}^{M} \frac{C_j Z_0^j R_j}{R_j + Z_0^j} \frac{\mathrm{d}q_{\text{out}}^j}{\mathrm{d}t},$$

$$C_T = C_c + C_p, \quad C_p = \sum_{j=1}^{M} \frac{R_j C_j}{R_j + Z_0^j}, \quad \frac{1}{R_T} = \sum_{j=1}^{M} \frac{1}{R_j + Z_0^j}, \tag{18}$$

where $q_{\text{OUT}}(t)$ is the total outflow through the terminal branches of the system, C_T and R_T are the total compliance and resistance, and C_p is the total peripheral compliance. The solution to Eq. 17 is

$$\tilde{p} - P_{\text{out}} = (\tilde{p}_0 - P_{\text{out}}) \mathrm{e}^{\frac{T_0 - t}{R_T C_T}} + \frac{\mathrm{e}^{\frac{-t}{R_T C_T}}}{C_T} \int_{T_0}^{t} \left(q_{\text{IN}}(t') + \sum_{j=1}^{M} \frac{C_j Z_0^j R_j}{R_j + Z_0^j} \frac{\mathrm{d}q_{\text{out}}^j(t')}{\mathrm{d}t'} \right) \mathrm{e}^{\frac{t'}{R_T C_T}} \mathrm{d}t', \quad t \geq T_0, \tag{19}$$

where $\tilde{p}_0 = \tilde{p}(T_0)$ is the pressure at the onset of the ejection, $t = T_0$ (Fig. 1, bottom right).

Equation 19 fails to reproduce the wave-like nature of pulse propagation because changes in pressure and flow rate are assumed to occur synchronously throughout the arteries. However, it is a good approximation to the pressure in the arterial network when wave activity is minimal, so that blood inertia can be neglected. According to [19,21] this is the case in approximately the last two thirds of diastole under normal conditions. During diastole the aortic valve is closed so $q_{\text{IN}} = 0$, which reduces Eq. 19 to

$$\tilde{p} - P_{\text{out}} = (\tilde{p}(T_N) - P_{\text{out}}) \mathrm{e}^{\frac{T_N - t}{R_T C_T}} + \frac{\mathrm{e}^{\frac{-t}{R_T C_T}}}{C_T} \sum_{j=1}^{M} \frac{C_j Z_0^j R_j}{R_j + Z_0^j} \int_{T_N}^{t} \frac{\mathrm{d}q_{\text{out}}^j(t')}{\mathrm{d}t'} \mathrm{e}^{\frac{t'}{R_T C_T}} \mathrm{d}t', \quad T_N \leq t \leq T_f, \tag{20}$$

where $\tilde{p}(T_N)$ is the pressure $\tilde{p}$ at the start of diastole $(t = T_N)$ and T_f is the time at which the heartbeat ends, as shown in Fig. 1 (top right). Equation 20 shows that, if viscous resistance to flow and blood inertia can be neglected in large arteries, the diastolic pressure decay depends on the global conditions C_T, R_T and P_{out}.

Note that if $C_j = 0$ $(j = 1, \ldots, M)$ in Eq. 16, then the lumped parameter model described by Eq. 17 leads to the windkessel equation proposed by Frank [22]; i.e.

$$q_{\text{IN}} = \frac{\tilde{p} - P_{\text{out}}}{R_T} + C_p \frac{\mathrm{d}\tilde{p}}{\mathrm{d}t}, \tag{21}$$

whose solution during diastole $(q_{\text{IN}} = 0)$ is

$$\tilde{p} - P_{\text{out}} = (\tilde{p}(T_N) - P_{\text{out}}) \mathrm{e}^{\frac{T_N - t}{R_T C_c}}, \quad T_N \leq t \leq T_f. \tag{22}$$

Integration of Eq. 17 over a cardiac cycle $T_0 \leq t \leq T_f$ yields

$$\left(\overline{q}_{\text{IN}} - \overline{q}_{\text{OUT}}\right) T = C_T \left[\tilde{p}(T_f) - \tilde{p}(T_0)\right], \tag{23}$$

where

$$\overline{q}_{\mathrm{IN}} = \frac{1}{T}\int_{T_0}^{T_f} q_{\mathrm{IN}}\,\mathrm{d}t, \quad \overline{q}_{\mathrm{OUT}} = \frac{1}{T}\int_{T_0}^{T_f} q_{\mathrm{OUT}}\,\mathrm{d}t$$

are the mean values of q_{IN} (cardiac output) and q_{OUT} over the interval $[T_0, T_f]$, respectively, and $T = T_f - T_0$ is the period of the heartbeat. If the flow is periodic with a period T, Eq. 23 reduces to

$$\overline{q}_{\mathrm{IN}} = \overline{q}_{\mathrm{OUT}} = \frac{\overline{\tilde{p}} - P_{\mathrm{out}}}{R_T}, \tag{24}$$

where

$$\overline{\tilde{p}} = \frac{1}{T}\int_{T_0}^{T_f} \tilde{p}\,\mathrm{d}t.$$

3.3 Separation of the effects of peripheral dynamics

We now wish to separate the pressure and flow waveforms at any location in the arterial network into a contribution resulting from the peripheral flow dynamics and a contribution resulting from the propagation of the pulse wave imposed at the root and its reflections at the arterial junctions and aortic valve (referred to as 'conduit dynamics'). This separation can be achieved by enforcing terminal boundary conditions that completely absorb any incident wave, i.e. single resistances with $R = Z_0$, according to (10).

Figure 3 (left) shows that the largest contribution of the conduit component of pressure to the pressure waveform at the thoracic aorta of the 55-arteries model occurs during the early systolic rise. Later in the cardiac cycle, the peripheral component becomes dominant, which highlights the importance of the peripheral flow dynamics to produce the diastolic decay. Overall, the peripheral component has a larger contribution to the pressure waveform than does the conduit component. Nevertheless, the conduit component is responsible for the dicrotic notch.

The conduit component of the flow waveform is dominant during most of the systolic period, whereas the peripheral component causes the reverse flow at the end of systole and dictates the total flow during approximately the last two thirds of diastole (Fig. 3, right). This pattern of conduit and peripheral components of the flow repeats every cardiac cycle from the beginning of the simulation. However, Fig. 4 highlights that there is a transient in the pressure waveform over multiple cycles, which is dictated by the peripheral component of pressure. According to Eq. 23, this transient is the result of the cardiac output $\overline{q}_{\mathrm{IN}}$ being larger than the total outflow $\overline{q}_{\mathrm{OUT}}$. The flow volume remaining in the arterial system increases $\tilde{p}$ at the end of each cardiac cycle by a magnitude that depends on

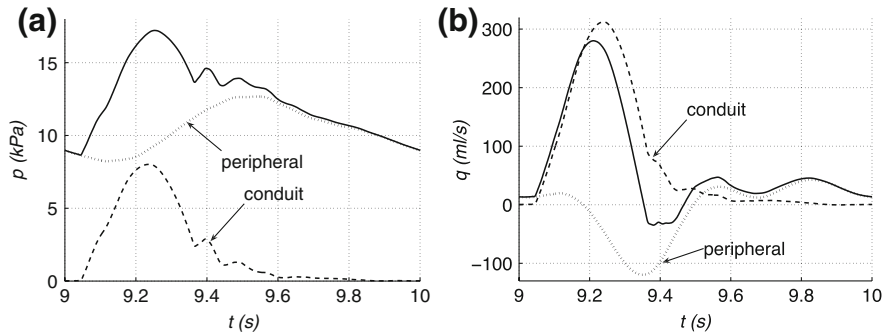

Fig. 3 Pressure (*left*) and flow (*right*) waveforms (*solid lines*) in the midpoint of the thoracic aorta (segment 27) separated into conduit and peripheral components once the flow has reached a periodic state

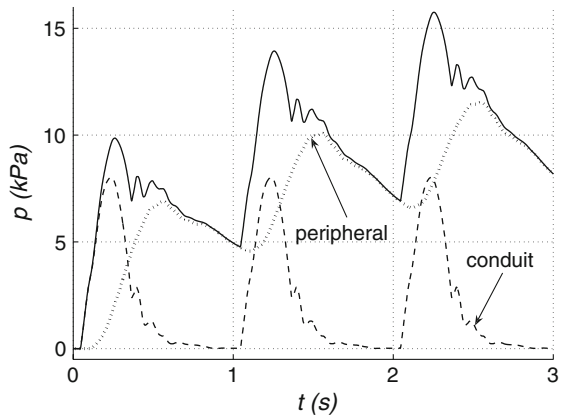

Fig. 4 Total (*solid line*) pressure waveform and its conduit and peripheral components in the midpoint of the thoracic aorta (segment 27) during the first three cardiac cycles after starting the heart from rest

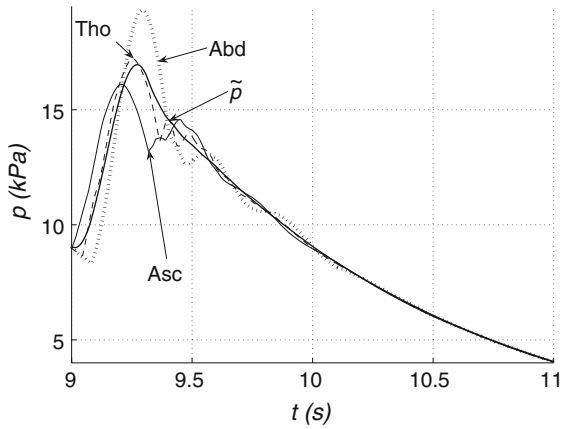

Fig. 5 Pressures at the root of the ascending aorta (Asc), and the midpoints of the thoracic aorta II (Tho) and abdominal aorta IV (Abd). The *solid line* shows the space-independent pressure $\tilde{p}$ obtained using Eq. 19 with $T_0 = 0$ and $\tilde{p}_0 = 0$. The periodic inflow rate in Fig. 1 (*top right*) was imposed until $t = 10\,\text{s}$. For $t > 10\,\text{s}$, $q_{\text{IN}} = 0$

the ratio T/C_T. In our model it takes approximately six cardiac cycles to reach a periodic flow with $\overline{q}_{\text{IN}} = \overline{q}_{\text{OUT}}$. At that time, the mean pressure everywhere in the 1-D model arteries is $\overline{\tilde{p}} = 12.5\,\text{kPa}$, which is in agreement with the value dictated by Eq. 24.

The results reported for the thoracic aorta apply to any other arterial segment in the model. Figure 5 shows that the differences between the exponential decay dictated by Eq. 19 (with $R_T C_T = 1.3$ s) and the pressures simulated using the 1-D model at different locations along the aorta decrease towards the last part of diastole. This pressure behaviour suggests that Eq. 20 provides a good description of pressure during the last part of diastole and, hence, wave activity is decreasing during diastole.

4 Aortic-valve dynamics

The hyperbolic nature of system (4) allows us to prescribe either a pressure $p_{\text{root}}(t)$ or a flow rate $q_{\text{root}}(t)$ at the inlet of the ascending aorta through the solution of a Riemann problem (Fig. 6). An intermediate state (p^*, q^*) originates at time $t + \Delta t$ (Δt is an arbitrary small time interval) from the states (p_L, q_L) and (p_R, q_R) at time t. In our model the state (p_R, q_R) corresponds to the solution at the beginning of the 1-D domain, and (p_L, q_L) is a virtual state selected so that $p^* = p_{\text{root}}$ or $q^* = q_{\text{root}}$. According to (8),

$$p^* = \frac{w_f - w_b}{2} Z_0, \quad q^* = \frac{w_f + w_b}{2}, \tag{25}$$

with $w_f = q_L + p_L/Z_0$ and $w_b = q_R - p_R/Z_0$, which leads to $2q^* = q_L + q_R + (p_L - p_R)/Z_0$. We can, therefore, prescribe q_{root} using $p_L = p_R$ and $q_L = 2q_{\text{root}} - q_R$, which yields $q^* = q_{\text{root}}$ and $p^* = Z_0(q_{\text{root}} - w_b)$. Note that $p^* \neq Z_0 q^*$ unless $w_b = 0$ (i.e. no waves arrive at the inlet from the periphery). This is the case at the beginning of the systolic ejection [25].

When $w_b \neq 0$, any perturbation $(\delta p, \delta q)$ propagating in the backward direction of the 1-D domain (i.e. $w_f = 0$ and $\delta p = -Z_0 \delta q$) produces a reflected state $(\delta p^*, \delta q^*)$ that satisfies $\delta q^* = q_{\text{root}}$ and $\delta p^* = Z_0 q_{\text{root}} + 2\delta p$. Following the notation used in the acoustics and surface waves literature [23, Chap. 8], we define the reflection coefficient at the aortic valve, R_v, as the ratio of the pressure change associated with the reflected wave to that of the incident wave; i.e.

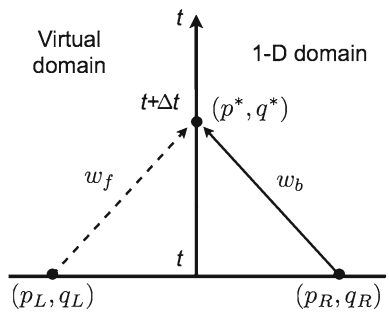

Fig. 6 Notation for the Riemann problem at the inlet of the ascending aorta

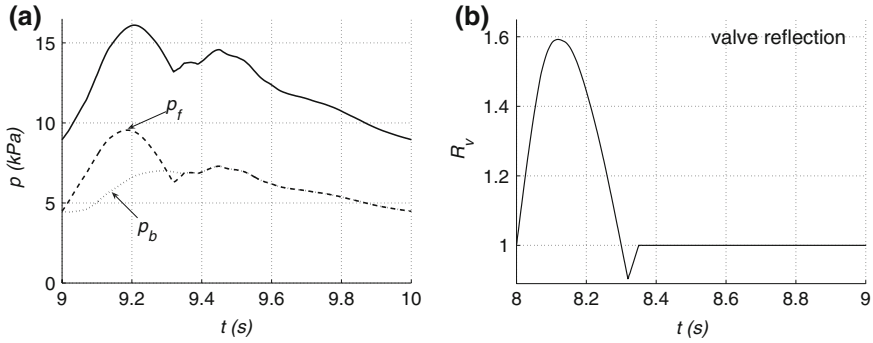

Fig. 7 Pressure (*solid line*) with its forward (p_f) and backward (p_b) travelling components (*left*), and reflection coefficient (*right*) at the inlet of the ascending aorta

$$R_v = \frac{\delta p^* - \delta p}{\delta p} = \frac{\delta q - \delta q^*}{\delta q} = -\frac{w_f}{w_b}. \tag{26}$$

Substituting $\delta q^* = q_{\text{root}}$ in Eq. 26 leads to

$$R_v = 1 - \frac{q_{\text{root}}}{\delta q}, \tag{27}$$

where $R_v > 1$ or $R_v < 1$ depending on the ratio $q_{\text{root}}/\delta q$, and $R_v = 1$ if $q_{\text{root}} = 0$. If $w_b \neq 0$, combination of Eqs. 9 and 26 leads to the following relation between the forward and backward components of pressure and flow rate at the inlet of the network

$$p_f = R_v p_b, \quad q_f = -R_v q_b. \tag{28}$$

The equations of (28) tell us that p and q at the inlet depend on the state of the valve (R_v) and on the pulse waves coming from peripheral locations.

If p_{root} is prescribed (using $q_L = q_R$ and $p_L = 2p_{\text{root}} - p_R$) instead of q_{root}, a similar analysis shows that

$$R_v = \frac{p_{\text{root}}}{\delta p} - 1. \tag{29}$$

Figure 7 (left) indicates that p_f at the inlet of the ascending aorta of the 55-arteries model contains a notch at the end of systole unlike p_b. The shape of p_f during systole depends on the shapes of R_v and p_b (Fig. 7, right) through (28), which shows that the dicrotic notch is sharpened by the notch in R_v. According to Eq. 27, $R_v < 1$ at the end of systole because both q_{root} and δq are negative. The reverse flow in q_{root} (Fig. 1, top right) is caused by the suction generated after the closure of the valve [24, Chap. 11].

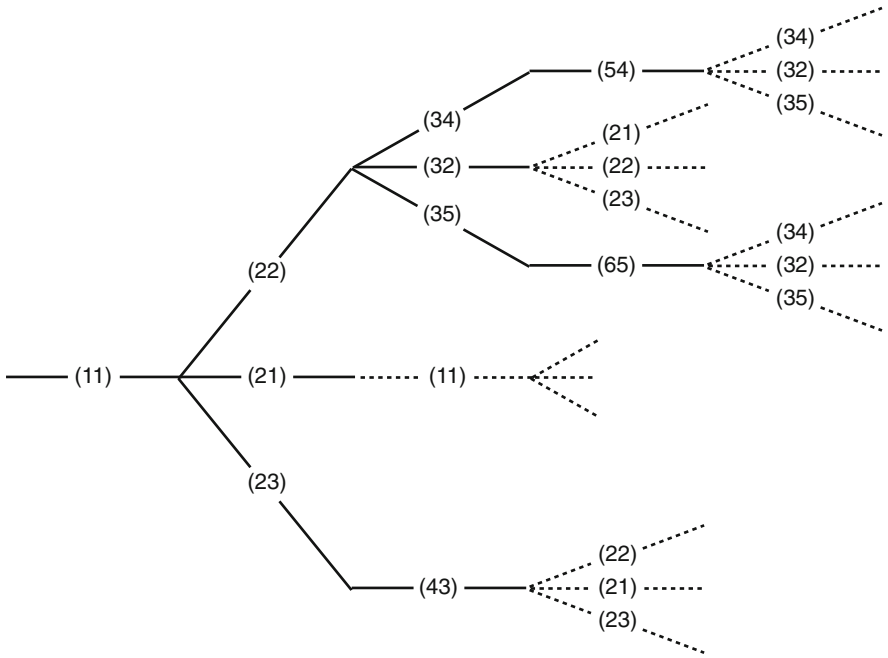

Fig. 8 Tree of waves generated by a single wave starting at the root of the bifurcating tree in Fig. 2 (*left*). The dotted branches indicate points of iteration in the tree, i.e. waves that have already appeared in the tree. The wave on each branch is indicated by (ne), where n is the node at which the wave originated and e is the edge along which it is travelling

5 Conduit dynamics

Section 5.1 describes the wave tracking algorithm used to analyse the conduit components of pulse waveforms in a 1-D model arterial network. Section 5.2 discusses the application of this algorithm to the simple networks shown in Fig. 2 and Sect. 5.3 to the 55-arteries model shown in Fig. 1.

5.1 Wave-tracking algorithm

We consider the arterial system to be a network of uniform tubes with N nodes and E edges.[3] All nodes are assumed to be either of degree $d = 1$ (external nodes with one edge) or $d = 3$ (internal nodes with three edges). A wave arriving at an internal node will generate three new waves; a reflected wave in the same edge and two transmitted waves in the other two edges connected to that node. A wave arriving at an external node will generate only one wave; a reflection in the connected edge. Thus, the number of waves in the network will increase exponentially with the number of nodes m that are encountered, growing approximately as 3^m (it is less than 3^m because some of the nodes are external in the arterial system).

We now describe a way of monitoring the waves propagating in a network. We denote a wave with the syntax (ne) where n is the node at which the wave starts and e is the edge in which it is travelling. Each wave will have a history which is given by the sequence of waves $(ne)_i$ $(i = 1, \ldots, W)$ that produced it (W is the number of waves in the sequence). We will call this sequence the 'wave path'. To keep track of the possible wave paths through the network, we will use the concept of the 'tree of waves' introduced in [26]. Figure 8 shows the tree of waves for the bifurcating tree in Fig. 2 (left).

[3] Edges were previously called arterial segments that could taper and continuously reflect waves. We will now consider the case in which all the reflection sites of the network are concentrated in its nodes.

An arterial network will be described using the $N \times E$ incidence matrix, $\mathbf{B}$, containing -1 for the node at the start of an edge and $+1$ for the node at the end of the edge. This implies a direction for the network which we will take as the direction of the mean blood flow.

The incidence matrices for the bifurcating tree and single loop networks shown in Fig. 2 are

$$\mathbf{B} = \begin{bmatrix} -1 & 0 & 0 & 0 & 0 \\ 1 & -1 & -1 & 0 & 0 \\ 0 & 1 & 0 & -1 & -1 \\ 0 & 0 & 1 & 0 & 0 \\ 0 & 0 & 0 & 1 & 0 \\ 0 & 0 & 0 & 0 & 1 \end{bmatrix}, \quad \mathbf{B} = \begin{bmatrix} -1 & 0 & 0 & 0 & 0 & 0 & 0 & 0 \\ 1 & -1 & -1 & 0 & 0 & 0 & 0 & 0 \\ 0 & 1 & 0 & -1 & -1 & 0 & 0 & 0 \\ 0 & 0 & 1 & 0 & 0 & -1 & -1 & 0 \\ 0 & 0 & 0 & 1 & 0 & 0 & 0 & 0 \\ 0 & 0 & 0 & 0 & 1 & 1 & 0 & -1 \\ 0 & 0 & 0 & 0 & 0 & 0 & 1 & 0 \\ 0 & 0 & 0 & 0 & 0 & 0 & 0 & 1 \end{bmatrix},$$

respectively. Note that each column of the incidence matrix sums to zero (one inlet and one outlet per edge) and that the sum of the absolute values of the rows give the degree of the node, 1 or 3.

Given the matrix $\mathbf{B}$ and an initial wave (ne), we can build the tree of waves using the following algorithm. Considering that the initial wave is the first generation of the tree of waves, for subsequent generations:

1. For each of the wave paths Ω calculated in the previous generation, get the last wave $(ne)_W$ and use the eth column of $\mathbf{B}$ to determine the other node of edge e, n', towards which $(ne)_W$ is travelling. Use the n'th row of $\mathbf{B}$ to determine the degree, d, of n'.
2. If $d = 1$ (external node), generate a new wave path Ω' with the same history of waves as Ω plus a new wave $(n'e)_{W+1}$; i.e. $[\Omega, (n'e)_{W+1}]$. Else ($d = 3$, internal node), generate three new wave paths Ω'_i ($i = 1, \ldots, 3$) with the same history of waves as Ω plus a new wave $(n'e_i)_{W+1}$; i.e. $[\Omega, (n'e_i)_{W+1}]$ ($i = 1, \ldots, 3$). The edges e_i will be those connected to the node n', which can be determined from the n'th row of $\mathbf{B}$.

Note that the computation of the tree of waves will never end and so we limit the waves generated to those whose net time of travel is smaller than a given time (e.g. one cardiac cycle).

Once we know all the wave paths generated in a network, we can calculate the time of travel (Sect. 5.1.1) and pressure (Sect. 5.1.2) of their final waves $(ne)_W$. Combination of these times and pressures yields the pressure and flow rate time histories at a location x_e in an edge e (Sect. 5.1.3).

5.1.1 Time of travel of a wave path

Given the wave path $(ne)_i$ ($i = 1, \ldots, W$), we define the 'time of travel' τ as

$$\tau = \sum_{i=1}^{W} (\tau_e)_i, \tag{30}$$

where $(\tau_e)_i = l_e/c_e$ is the time of transit of the wave $(ne)_i$ ($i = 1, \ldots, W$), with l_e and c_e the length and wave speed of edge e. The time of arrival of the last wave $(ne)_W$ at a location x_e in edge e, denoted τ_{x_e}, is

$$\begin{aligned} \tau_{x_e} &= \tau - (1 - x_e/l_e)(\tau_e)_W, && \text{if } \mathbf{B}(n,e) = -1, \\ \tau_{x_e} &= \tau - (x_e/l_e)(\tau_e)_W, && \text{if } \mathbf{B}(n,e) = 1. \end{aligned}$$

5.1.2 Pressure of a wave path

A wave arriving at an external node will be reflected with a reflection coefficient that is determined by the properties of the edge and the properties of the vessels outside of the network that are connected to the node. We assume that these reflection coefficients, which are typically part of the boundary conditions, are known. The reflection

coefficients at the internal nodes depend upon the properties of the edges connected to the node and the edge from which the wave approaches the node. Consider the internal node n connecting the edges a, b and c. The reflection coefficient for a wave approaching in edge j ($j = a, b, c$) will be designated R_{jn}. According to the linear 1-D formulation, the three reflection coefficients at this node are [10]

$$R_{an} = \frac{Y_a - Y_b - Y_c}{Y_a + Y_b + Y_c}, \quad R_{bn} = \frac{Y_b - Y_c - Y_a}{Y_b + Y_c + Y_a}, \quad R_{cn} = \frac{Y_c - Y_a - Y_b}{Y_c + Y_a + Y_b}, \tag{31}$$

where $Y = A_0/\rho c_0$ is the admittance of the edge (the subscripts denote the edge number). The transmission coefficients for the waves transmitted into the other two edges connected to the node n will be designated by T_{jn}. They are $T_{jn} = R_{jn} + 1$. Since Y is real and positive, R_{jn} are bounded by -1 and $+1$. The limit -1 is for a vessel with an open end and the limit $+1$ is for a vessel with a closed end. The case $R_{jn} = 0$ is for a vessel with a well-matched end. The coefficients T_{jn} are bounded by 0 and 2.

Given a wave path $(ne)_i$ ($i = 1, \ldots, W$), we observe that the pressure $\mathcal{P}$ of its final wave is given by

$$\mathcal{P} = \prod_{i=1}^{W-1} (RT)_i, \tag{32}$$

where $(RT)_i = R_{en'}$ if $(ne)_i$ is travelling towards an external node n', or $(RT)_i = T_{en'}$ if $(ne)_i$ is travelling towards an internal node n'. For instance, $\mathcal{P} = T_{12}T_{23}T_{56}R_{88}T_{86}T_{64}T_{32}$ for the wave path (11)(22)(35)(68)(88)(66)(43)(21) in the single loop network of Fig. 2 (right), assuming that the magnitude of the initial wave (11) is 1 (in pressure units).

5.1.3 Pressure and flow time histories

We first show how to obtain the discrete pressure time history, $\mathcal{T}_P(x_e, t)$, at a location x_e in an edge e produced by a single pulse wave propagating from the root at time $t = 0$; i.e. the system is excited with the input

$$p(t) = \delta(t) = \begin{cases} 1 & \text{if } t = 0, \\ 0 & \text{if } t \neq 0. \end{cases} \tag{33}$$

This wave will generate a combinatorial number Γ_e of wave paths with their last wave travelling in edge e. As the wave paths lengthen, the number $\Gamma_\tau < \Gamma_e$ of wave paths Ω_i ($i = 1, \ldots, \Gamma_\tau$) with the same τ_{x_e} increases, since τ does not depend upon the sequence of edges (Eq. 30). Therefore, the total pressure at x_e at $t = \tau_{x_e}$ will be

$$\mathcal{T}_P(x_e, \tau_{x_e}) = \sum_{i=1}^{\Gamma} \mathcal{P}_i, \tag{34}$$

where $\mathcal{P}_i$ is the pressure of the final wave of Ω_i ($i = 1, \ldots, \Gamma$). Note that $\mathcal{T}_P(x_e, \tau_{x_e})$ can be separated into the pressure time histories of the waves travelling forward, $\mathcal{T}_{P_f}(x_e, \tau_{x_e})$, and backward, $\mathcal{T}_{P_b}(x_e, \tau_{x_e})$, where

$$\begin{aligned} \mathcal{T}_{P_f} &= \sum_{i=1}^{\Gamma_f} \mathcal{P}_i, \quad \text{if } \mathbf{B}(n_i, e_i) = -1, \\ \mathcal{T}_{P_b} &= \sum_{i=1}^{\Gamma_b} \mathcal{P}_i, \quad \text{if } \mathbf{B}(n_i, e_i) = 1, \end{aligned} \tag{35}$$

n_i and e_i are the node and edge, respectively, of the last wave of Ω_i ($i = 1, \ldots, \Gamma$) and $\Gamma = \Gamma_f + \Gamma_b$.

Making use of the linear Riemann variables (7), we can relate $\mathcal{T}_{P_f}$ and $\mathcal{T}_{P_b}$ to the corresponding flow rate time histories $\mathcal{T}_{Q_f}$ and $\mathcal{T}_{Q_b}$. For a wave travelling in the forward direction, we have $w_b = 0$ and, hence, $q = p/Z_0$. For a wave travelling in the backward direction, we have $w_f = 0$ and, hence, $q = -p/Z_0$. Therefore,

$$\mathcal{T}_{Q_f} = \frac{\mathcal{T}_{P_f}}{Z_0}, \quad \mathcal{T}_{Q_b} = -\frac{\mathcal{T}_{P_b}}{Z_0}. \tag{36}$$

In digital signal processing terminology [27, Chap. 3], $\mathcal{T}_{P_f}$, $\mathcal{T}_{P_b}$, $\mathcal{T}_{Q_f}$, and $\mathcal{T}_{Q_b}$ are the 'transfer functions' that, convoluted with an input pressure enforced at the root of the network, give the forward and backward pressure and flow rate time histories at x_e, respectively, produced by the input pressure.

Table 3 Geometrical data of the bifurcating tree and single loop networks in Fig. 2

The last two columns show the reflection coefficients at the inlet and outlet of the edge, separated by a slash (tree/loop) if they differ in both networks. Waves propagate at a speed $c_0 = 5.6$ m/s in all edges

Edge	Length (cm)	Radius (mm)	R_{inlet}	R_{outlet}
1	50	5.0	−1.00	0.19
2	75	4.0	−0.24	0.11
3	100	1.0	−0.95	0.50/−0.86
4	125	0.8	−0.96	0.50
5	100	3.5	−0.15	0.50/−0.36
6	75	0.9	−0.88	−0.96
7	75	3.5	0.74	0.50
8	50	5.0	0.31	0.50

5.2 Application to simple networks

We first apply the wave tracking algorithm to calculate the pressure and flow transfer functions generated by a single wave starting at node 1 in the bifurcating tree and single loop networks (Fig. 2) at $t = 0$. The reflection coefficients of these networks are shown in Table 3. Figure 9 shows $\mathcal{T}_{P_f}$, $\mathcal{T}_{P_b}$, $\mathcal{T}_{Q_f}$, and $\mathcal{T}_{Q_b}$ in the midpoint of edge 1 of both networks during the first 2 s. After the initial wave has arrived at the measuring site, subsequent forward-travelling waves are the result of the reflection of backward-travelling waves at node 1, where the reflection coefficient is $R_{11} = -1$ (i.e. node 1 is an open end). Therefore, there is an equal number of forward waves with the same net time of travel as backward waves. This is the case for all the edges connected to an external node whose reflection coefficient is not zero.

In any edge, the number of waves with the same time of travel increases with the number of generations of the tree of waves. The total number of wave paths generated during $0 \leq t \leq 2$ s is 36,929 in the bifurcating tree network and 456,553 in the single loop network. In both cases, the total number of generations of the tree of waves is 24; i.e. $W = 24$ at most. More wave paths are generated in the loop network after approximately 0.7 s, because this network contains more reflection sites than the bifurcating tree and the loop multiplies the number of wave paths with the same number of waves. Although the simultaneous arrival of separate waves with the same time of travel can lead to an amplification of the total magnitude of pressure and flow, only a few waves (at most four) contribute $> 95\%$ of the corresponding total magnitudes of the results in Fig. 9.

The wave tracking algorithm allows us to determine the path history of all the waves arriving at a measurement site. For instance, the six backward-travelling waves at approximately $t = 0.75$ s in Fig. 9 (top left) followed the edges 1–2–2–3–3–1, 1–2–4–4–2–1, 1–3–3–2–2–1, 1–1–1–1–1–2–2–1, 1–1–1–2–2–1–1–1, and 1–2–2–1–1–1–1–1. Their pressures are 0.0023, 0.426, 0.0023, 0.0035, 0.0035 and 0.0035, respectively, of the pressure of the initial wave a $t = 0$.

5.3 Application to the 55-arteries model

We now apply the wave tracking algorithm to analyse the conduit component of the pressure waveforms obtained in Sect. 3.3. The reflection coefficients at the internal nodes of the 55-arteries model is shown in Table 1. Zero reflection coefficients have been considered at all the external nodes. Only waves with a pressure larger than 0.001 of the pressure of the initial wave at the ascending aorta are computed.

Figure 10 (top) shows an increase of 62% in the pressure of the initial wave that propagates from the inlet of the ascending aorta to the midpoint of the thoracic aorta. This result is in accordance with the transmission coefficients encountered on the way from edge 1 to edge 27 through edges 2, 14 and 18. The number of the waves produced

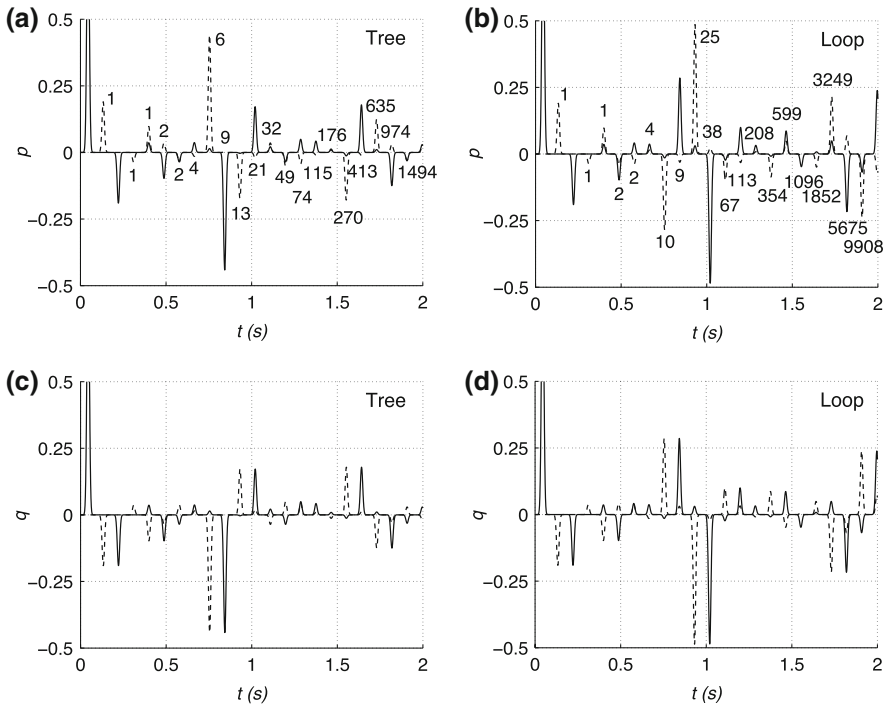

Fig. 9 Forward (*solid lines*) and backward (*dashed lines*) travelling pressures (*top*) and flows (*bottom*) in the midpoint of edge 1 of the bifurcating tree (*left*) and single loop (right) networks (Fig. 2) generated by a delta wave (which is truncated in the plots) starting at node 1 when $t = 0$. They were calculated using the wave tracking algorithm. The delta waves are represented by Gaussian functions with a small variance for ease of presentations. The numbers indicate the total number of wave paths with the same time of travel coming from node 2 that combine to produce the backward-travelling waves. Pressures and flows are nondimensionalised by the corresponding values of the initial wave coming from node 1

by the reflection of the initial wave increases approximately as 3^m, with m being the number of internal nodes encountered. As a result, there is an increase in the number of wave paths with the same net time of travel, whose combined pressure can take positive and negative values (Fig. 10, bottom left). However, the absolute values of these pressures tend to decrease exponentially. The wave tracking algorithm allows us to isolate those wave paths that have visited a particular vessel, the right carotid artery in this particular example, whose pressures also tend to decrease exponentially (Fig. 10, bottom right).

Convolution of the pressure transfer function ($\mathcal{T}_{P_f} + \mathcal{T}_{P_b}$) shown in Fig. 10 (top) with p_f at the inlet of the ascending aorta (Fig. 11, left) yields the conduit component of pressure in the midpoint of the thoracic aorta II (Fig. 11, right). This result has been validated with the corresponding thoracic pressure obtained using the discontinuous Galerkin scheme (Fig. 3, left). Note that in this study we impose a forward-travelling pressure, p_f, which already accounts for the reflection of p_b at R_v and, hence, the external node in edge 1 was set to absorb any incident wave (unlike the reflective boundary dictated by Eq. 27 and considered in Sect. 3.3). The form of p_f is evaluated by executing the computational model with the inflow condition given in Fig. 1 (top right) and monitoring the forward pressure wave necessary to enforce this condition. This p_f simplifies the wave tracking analysis because it reduces the number of waves generated, but does not consider the influence of internal reflections as compared with reflections from the aortic valve. Figure 11 (right) shows that direct transmission of p_f from the inlet of the ascending aorta to the thoracic aorta through the aortic arch contributes most of the conduit component of pressure at the thoracic aorta. Pressure contributions from more distal reflection sites, such as the carotids, are smaller and they can take positive or negative values.

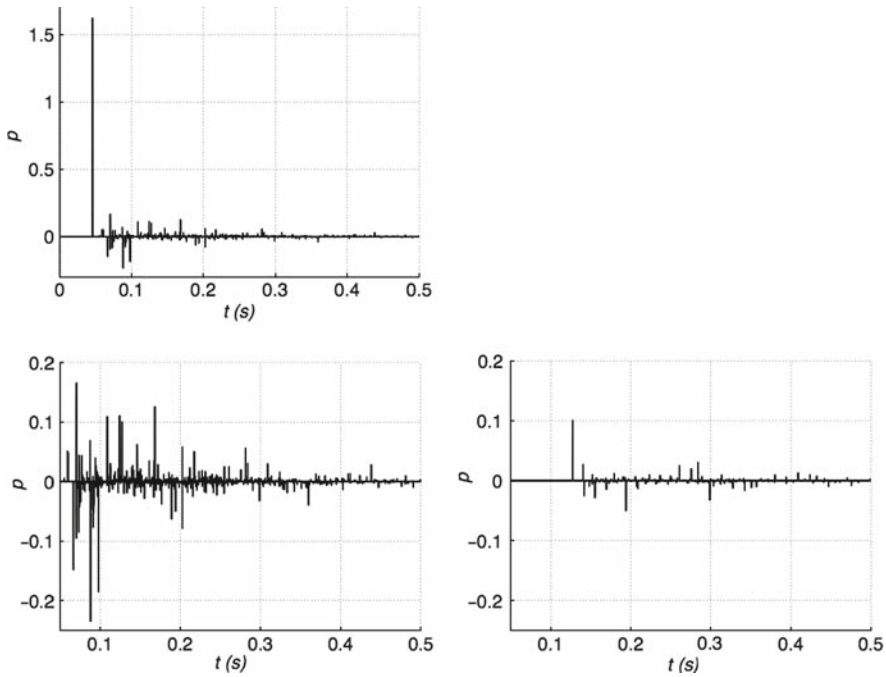

Fig. 10 (*top*) Pressure ($\mathcal{T}_{P_f} + \mathcal{T}_{P_b}$) in the midpoint of the thoracic aorta (edge 27) of the 55-arteries model generated by a single wave starting at the inlet of the ascending aorta (edge 1) when $t = 0$. It was calculated using the wave tracking algorithm with zero reflection coefficients at the external nodes. (*bottom*) Zoom of the reflections after the arrival of the initial wave (*left*) and of the reflections whose wave paths contain the node at the outlet of the right common carotid (edge 5) (*right*). All pressures are nondimensionalised by the initial pressure in edge 1

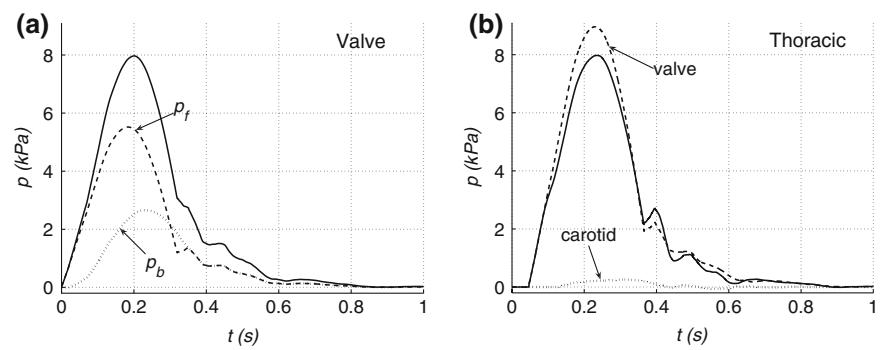

Fig. 11 (*left*) Conduit component of pressure (*solid line*) and its forward (p_f) and backward (p_b) travelling components at the inlet of the ascending aorta (edge 1). They were obtained using the discontinuous Galerkin scheme. (*right*) Conduit component of pressure (*solid line*) in the midpoint of the thoracic aorta (edge 27) obtained by convoluting p_f with the transfer function $\mathcal{T}_{P_f} + \mathcal{T}_{P_b}$ in the midpoint of edge 27 (Fig. 10, top). This panel also shows the result of convoluting p_f with the initial wave in Fig. 10 (top) ('valve') and with the part of the signal that contains all waves reflected at the outlet of the right carotid artery (Fig. 10, bottom right) ('carotid')

6 Discussion and concluding remarks

We have studied the mechanisms underlying the pattern of arterial pulse waves in the systemic arterial network in normal conditions, using a time-domain analysis of the linear and inviscid 1-D equations of blood flow in compliant vessels. These equations are based on the physical principles of conservation of mass and balance of momentum. The assumptions of linearity and inviscid flow make the analysis simpler. They are justified because nonlinearities, such as the convective term in Eq. 2 and the dependence of the wave speed on pressure, do not produce

significant changes in the features of pulse waveforms studied in this work. Viscous dissipation in the large arteries can be neglected because the greatest fall in mean pressure occurs in the arterioles downstream the arterial network [24, Chap. 12].

Our work has focused on separating and analysing the flow dynamics at the flow out of the left ventricle (aortic valve) and at the conduit and peripheral reflection sites of the arterial network. Understanding of the local and global effects on pulse waveforms of the resistances and compliances that model the perfusion of the microcirculation has allowed us to identify the peripheral contributions to the simulated pulse waveforms (Sect. 3 and Figs. 3 and 4). Overall, the peripheral component of the pressure waveform at an arbitrary arterial location makes a larger contribution than does the conduit component. The peripheral component is very nearly equal to the total pressure during the last part of diastole, when the conduit component is minimal and the pressure diastolic decay approaches a space-independent value $\tilde{p}(t)$. The pressure $\tilde{p}$, and hence the diastolic pressure decay, depend on the total compliance C_T and the total peripheral resistance R_T of the arterial network, and the pressure P_{out} at which flow to the venous system ceases (Eq. 20 and Fig. 5).

These results suggest that wave activity is vanishing towards the end of diastole, which is in agreement with previous studies involving human and canine in vivo data [19–21]. Nevertheless, the pulse waves generated by the contraction of the left ventricle have to produce both the conduit and peripheral components of pressure, since they are the only supply of energy into the system. The conduit component is independent of the transient undergone by pressure in the first few cardiac cycles (Fig. 4). Consequently, it is the peripheral component that brings the blood flow towards the steady-state oscillation dictated by the cardiac output ($\bar{q}_{\text{IN}}$), R_T and P_{out} through Eq. 24. In this state, $\bar{q}_{\text{IN}}$ is equal to the mean value of the total peripheral outflow $\bar{q}_{\text{OUT}}$ in one cardiac cycle (of duration T), and the mean pressure $\bar{\tilde{p}}$ in each cardiac cycle depends on $\bar{q}_{\text{IN}}$, R_T and P_{out} only. The ratio T/C_T dictates the rate at which the flow approaches this steady-state oscillation (Eq. 23). We can conclude that pulse wave propagation is the mechanism by which the arterial system reaches the mean pressure dictated by $\bar{q}_{\text{IN}}$, R_T and P_{out} that is required to perfuse the microcirculation. Conduit and distal compliances determine the rate at which this pressure is restored when the system has departed from its equilibrium state of steady oscillation.

The analysis of the reflection coefficient at the aortic valve has shown that pulse waveforms are closely related to the outflow from the left ventricle in early systole. Later in systole, they depend on reflections at the junctions of the arterial network and the aortic valve. We have shown that the reflection coefficient at the aortic valve changes with time and its pattern is close to the shape of the flow at the inlet of the ascending aorta (Eq. 27 and Fig. 7). During systole, it is larger than 1, it becomes smaller than 1 when the valve is closing, and it is equal to 1 when the valve is closed. The resulting notch in the reflection coefficient sharpens the dicrotic notch. It is the suction generated after the closure of the valve [24, Chap. 11] that leads the reverse flow at the ascending aorta (Fig 1, top right) and, hence, the notch in the reflection coefficient.

The wave-tracking algorithm that we have proposed to study the reflections at the junctions of the arterial network assumes constant arterial diameters between branches, so that the arterial network is represented using a network of edges and nodes. According to [28], this representation is a good approximation to physiological diameters. The algorithm can be applied to arterial networks with terminal branches coupled to peripheral resistances, which relate the flow to pressure without any time delay and can be expressed as a reflection coefficient using (10). Networks with other types of terminal boundary conditions (e.g. peripheral windkessel models) can also be analysed using the wave-tracking algorithm. We first need to separate the peripheral components and then apply the algorithm to the conduit components.

Figures 3 and 4 show that the conduit component of pressure is responsible for the dicrotic notch in the pressure waveforms obtained in a 1-D model of the largest 55 arteries in the human. Application of the wave-tracking algorithm to study the conduit components of this system has shown that there are multiple reflection sites in the arterial network. As a result, the number of reflected waves increases exponentially as the cardiac cycle progresses. Moreover, reflected waves get trapped in the arterial network, within the closed aortic valve and the peripheral vessels. According to [28,29], arterial bifurcations are close to well matched for forward-travelling waves in normal conditions. However, the reflection coefficients in (31) show that the same bifurcations have to be poorly matched for backward-travelling waves [10]. As a result, waves get trapped on their way back to the heart. The total pressure

of simultaneous waves can be positive or negative, but its absolute value tends to decrease exponentially leading to minimal wave activity during the last part of diastole (Fig. 10). This result is in agreement with the space-independent pressure described by Eq. 19 to which the flow tends during diastole (Fig. 5).

This work has elucidated the mechanisms that relate the patterns of pulse waves to the flow out of the left ventricle, the geometry and compliance of the arterial network, and the flow dynamics in the peripheral vessels. We have shown that aortic pressure waveforms are closely related to the outflow from the left ventricle and to reflections at the arterial junctions and aortic valve during systole. These mechanisms produce the dicrotic notch. Wave activity decreases during diastole and, hence, the diastolic pressure decay approaches an uniform value that depends on the cardiac output and the total compliance and peripheral resistance. The cardiac output and total peripheral resistance dictate the mean pressure required to perfuse the microcirculation, and the total compliance determines the time it takes to reach this pressure.

The tools provided in this work could be applied to elucidate the physical parameters that should be monitored to diagnose disease (such as hypertension) and those that should be targeted to prevent and treat disease. Moreover, these tools can allow us to assess if pulse waveforms carry sufficient information to infer vascular anatomies (e.g. the circle of Willis in the cerebral circulation, which frequently presents anatomical variations) from non-invasive measurements, and to improve the efficacy of current tools for determining local wave speeds from simultaneous pressure and flow measurements [25,30].

Acknowledgements This work was supported by an EPSRC Advanced Research Fellowship, EP/C539834/1, and associated grant, EP/C539842/1.

References

1. Olufsen MS, Peskin CS, Kim WY, Pedersen EM, Nadim A, Larsen J (2000) Numerical simulation and experimental validation of blood flow in arteries with structured-tree outflow conditions. Ann Biomed Eng 28:1281–1299
2. Steele BN, Wan J, Ku JP, Hughes TJR, Taylor CA (2003) In vivo validation of a one-dimensional finite-element method for predicting blood flow in cardiovascular bypass grafts. IEEE Trans Biomed Eng 50:649–656
3. Alastruey J (2006) Numerical modelling of pulse wave propagation in the cardiovascular system: development, validation and clinical applications. Ph.D. thesis, Imperial College London, University of London
4. Matthys KS, Alastruey J, Peiró J, Khir AW, Segers P, Verdonck PR, Parker KH, Sherwin SJ (2007) Pulse wave propagation in a model human arterial network: assessment of 1-D numerical simulations against in vitro measurements. J Biomech 40:3476–3486
5. Hughes TJR, Lubliner J (1973) On the one-dimensional theory of blood flow in larger vessels. Math Biosci 18:161–170
6. Pedley TJ (1980) The fluid mechanics of large blood vessels. Cambridge University Press, Cambridge, UK
7. Smith NP, Pullan AJ, Hunter PJ (2001) An anatomically based model of transient coronary blood flow in the heart. SIAM J Appl Math 62:990–1018
8. Formaggia L, Lamponi D, Quarteroni A (2003) One-dimensional models for blood flow in arteries. J Eng Math 47:251–276
9. Čanić S, Kim EH (2003) Mathematical analysis of the quasilinear effects in a hyperbolic model blood flow through compliant axi-symmetric vessels. Math Method Appl Sci 26:1161–1186
10. Sherwin SJ, Franke VE, Peiró J, Parker KH (2003) One-dimensional modelling of a vascular network in space-time variables. J Eng Math 47:217–250
11. Alastruey J, Parker KH, Peiró J, Sherwin SJ (2008) Lumped parameter outflow models for 1-D blood flow simulations: effect on pulse waves and parameter estimation. Commun Comput Phys 4:317–336
12. Stergiopulos N, Young DF, Rogge TR (1992) Computer simulation of arterial flow with applications to arterial and aortic stenoses. J Biomech 25:1477–1488
13. Franke VE, Parker KH, Wee LY, Fisk NM, Sherwin SJ (2003) Time domain computational modelling of 1D arterial networks in monochorionic placentas. Math Model Numer Anal 37:557–580
14. Alastruey J, Parker KH, Peiró J, Sherwin SJ (2006) Can the modified Allen's test always detect sufficient collateral flow in the hand? A computational study. Comput Methods Biomech Biomed Eng 9:353–361
15. Alastruey J, Parker KH, Peiró J, Byrd SM, Sherwin SJ (2007) Modelling the circle of Willis to assess the effects of anatomical variations and occlusions on cerebral flows. J Biomech 40:1794–1805
16. Alastruey J, Moore SM, Parker KH, David T, Peiró J, Sherwin SJ (2008) Reduced modelling of blood flow in the cerebral circulation: coupling 1-D, 0-D and cerebral auto-regulation models. Int J Numer Methods Fluids 56:1061–1067
17. Formaggia L, Gerbeau JF, Nobile F, Quarteroni A (2001) On the coupling of 3D and 1D Navier–Stokes equations for flow problems in compliant vessels. Comput Methods Appl Mech Eng 191:561–582

18. Vignon-Clementel IE, Figueroa CA, Jansen KE, Taylor CA (2006) Outflow boundary conditions for three-dimensional finite element modeling of blood flow and pressure in arteries. Comput Methods Appl Mech Eng 195:3776–3796
19. Wang JJ, O'Brien AB, Shrive NG, Parker KH, Tyberg JV (2003) Time-domain representation of ventricular-arterial coupling as a windkessel and wave system. Am J Heart Circ Physiol 284:H1358–H1368
20. Davies JE, Hadjiloizou N, Leibovich D, Malaweera A, Alastruey J, Whinnett ZI, Manisty CH, Francis DP, Aguado-Sierra J, Foale RA, Malik IS, Parker KH, Mayet J, Hughes AD (2007) Importance of the aortic reservoir in determining the shape of the arterial pressure waveform—The forgotten lessons of Frank. Artery Res 1:40–45
21. Aguado-Sierra J, Alastruey J, Wang JJ, Hadjiloizou N, Davies JE, Parker KH (2008) Separation of the reservoir and wave pressure and velocity from measurements at an arbitrary location in arteries. Proc Inst Mech Eng Part H J Eng Med 222:403–416
22. Frank O (1899) Die Grundform des arteriellen Pulses. Z Biol 37:483–526
23. Lamb Sir H (1945) Hydrodynamics, Chap 8. Dover, New York, p 738
24. Caro CG, Pedley TJ, Schroter RC, Seed WA (1978) The mechanics of the circulation. Oxford University Press, Oxford
25. Khir AW, O'Brien A, Gibbs JSR, Parker KH (2001) Determination of wave speed and wave separation in the arteries. J Biomech 34:1145–1155
26. Wang JJ, Parker KH (2004) Wave propagation in a model of the arterial circulation. J Biomech 37:457–470
27. Lynn PA, Fuerst W (1989) Introductory digital signal processing with computer aplications. Wiley, New York
28. Suwa N, Niwa T, Fukasawa H, Sasaki Y (1963) Estimation of intravascular blood pressure gradient by mathematical analysis of arterial casts. Tohoku J Exp Med 79:168–198
29. Papageorgiou GL, Jones NB (1987) Arterial system configuration and wave reflection. J Biomed Eng 9:299–301
30. Davies JE, Whinnett ZI, Francis DP, Willson K, Foale RA, Malik IS, Hughes AD, Parker KH, Mayet J (2006) Use of simultaneous pressure and velocity measurements to estimate arterial wave speed at a single site in humans. Am J Physiol Heart Circ Physiol 290:H878–H885